PCCP

PAPER

View Article Online
View Journal | View Issue

Cite this: *Phys. Chem. Chem. Phys.*, 2025, **27**, 8202

X-ray absorption spectroscopy reveals charge transfer in π-stacked aromatic amino acids†

Carlos Ortiz-Mahecha, *[ab] Lucas Schwob, [b] Juliette Leroux, [bc] Sadia Bari, [bd] Robert H. Meißner *[ae] and Annika Bande *[fg]

Received 7th December 2024,
Accepted 20th March 2025

DOI: 10.1039/d4cp04615c

rsc.li/pccp

X-ray absorption spectroscopy (XAS) and quantum mechanical calculations bear great potential to unravel π stacking side-chain interaction properties and structure in, *e.g.*, proteins. However, core-excited state calculations for proteins and their associated interpretation for π–π interactions are challenging due to the complexity of the non-covalent interactions involved. A theoretical analysis is developed to decompose the core-to-valence transitions into their atomic contributions in order to characterize the π stacking of aromatic amino acids as a function of their non-covalent distance change. Three models were studied as a non-covalent mixed dimers of the phenylalanine, tyrosine and tryptophan amino acids. We found that there are carbon 1s → π* charge transfer transitions associated with the non-covalently paired aromatic amino acids through their side chains. The atomic-centered contributions to the electronic transition density quantify the excited state charge transfer of the pairing amino acid models, highlighting the π stacking interactions between their aromatic side chains.

Introduction

Non-covalent interactions between amino acids involving delocalized π-electrons play a key role in protein structure stabilization and biologic function.[1–3] Noteworthy, π–π stacking, OH–π, cation–π, and CH–π interactions mostly drive the coupling interactions in protein–ligand binding and tertiary structure formation.[2,4–6] In a protein structure, about 60% of the aromatic side chains interact in amino acid pairs, and about 80% of these pairs form aromatic–aromatic interactions with up to 7 Å separation.[1]

Understanding of the character of the π-electron interactions of amino acids with their chemical environment in peptides and proteins has been gained by means of X-ray absorption spectroscopy (XAS).[7–12] In XAS, resonant transitions arise from the promotion of inner-shell electrons to unoccupied valence orbitals, enabling the study of the local electronic structure. Thanks to the large differences in the electron binding energy of different atoms, XAS also allows probing those transitions in an element-specific manner.[13] In particular, the lowest lying excited states are indicative to some aspects of the molecular structure. In proteins and peptides, such excitations involve excited states having the promoted electron in a delocalized π* orbital.[14,15] Whenever π* orbitals are involved and the aromatic side chains are π–π stacked, the XAS signal will hence be affected. A site-specific distinction can thus take place for peptide bonds and aromatic side chain interactions. However, this distinction is complicated as each XAS peak arises from multiple carbon (C) 1s → π* transitions.[16,17]

Quantum-mechanical calculations are oftentimes used to provide an extended interpretation of experimental XAS spectra.[14,18–21] In the context of π stacking, characterization has been carried out both experimentally and computationally for small systems such as aromatic bicyclic and heterocyclic compounds.[22–26] However, the protein C 1s → π* transition intensities associated to π stacking occur at similar energies than other π-interaction related excitations such as those including the carbon of the carboxylic group, which makes it difficult to study only the distance effect of the first ones. We, therefore, developed a theoretical analysis as a means to differentiate the XAS transitions affected by the intermolecular π–π interactions between side chains of aromatic amino acids from other π–π related XAS transitions. With that we study the π stacking distance dependence of the C 1s → π* transition

[a] *Institute for Interface Physics and Engineering, Hamburg University of Technology, Hamburg, Germany. E-mail: robert.meissner@tuhh.de*
[b] *Deutsches Elektronen-Synchrotron DESY, 22603 Hamburg, Germany*
[c] *CIMAP, CEA/CNRS/ENSICAEN/Université de Caen Normandie, 14050 Caen, France*
[d] *Zernike Institute for Advanced Materials, University of Groningen, 9747 AG Groningen, The Netherlands*
[e] *Helmholtz-Zentrum Hereon, Institute of Surface Science, 21502 Geesthacht, Germany*
[f] *Institute of Inorganic Chemistry, Leibniz Hannover University, 30167 Hannover, Germany*
[g] *Theory of Electron Dynamics and Spectroscopy, Helmholtz-Zentrum Berlin für Materialien und Energie GmbH, 14109 Berlin, Germany. E-mail: annika.bande@helmholtz-berlin.de*

† Electronic supplementary information (ESI) available. See DOI: https://doi.org/10.1039/d4cp04615c

density matrix elements. For this work, we constructed a molecular model of an isolated pair of aromatic amino acids that allows to characterize the change in C 1s → π* transitions when the aromatic π–π stacking changes. Using our in-house analysis, we quantify the charge-transfer core excitations of the π–π stacking of aromatic amino acids.

Theory

A theoretical analysis of the π–π interaction was performed on a model comprising two different aromatic amino acids, namely all pairs of phenylalanine (Phe), tyrosine (Tyr) and tryptophan (Trp). It centered around the lowest-energy charge-transfer excited states, transition dipole moments and energy, as well as the Löwdin population to identify the C 1s → π* resonant transitions associated to the π stacking of the aforementioned systems. With a ground state energy decomposition analysis, the excited state properties of certain atom groups were ascribed to the intermolecular ground-state charge transfer energy for the same molecular fragment.

Chemical model construction

The chemical model consists of pairs of π-stacked amino acids to study their non-covalent interactions and was constructed by pairing the isolated aromatic amino acids—phenylalanine (Phe), tryptophan (Trp) and tyrosine (Tyr)—using the Dunbrack rotamer library.[27] Explicitly, the pairs Phe and Tyr (FY), Phe and Trp (FW), and Tyr and Trp (YW) are investigated. The distance in this model is defined as the intermolecular separation between the two parallely-stacked arene side chains, ranging from 3.5 up to 11.0 Å, as shown in Fig. 1A, with a 0.1 Å step size from 3.5 to 8.0 Å and a 0.5 Å step size from 8.0 to 11.0 Å.‡ Previously, other distance effects of parallel stacked arenes have been studied theoretically,[28–30] considering that the cofacial arrangement established the strongest π-atomic orbital overlap.[31–33] Although the face-to-face ring alignment is rarely reported experimentally,[34] it has been shown that the cofacial arrangement could facilitate the intermolecular charge transfer.[35–38] Such a cofacial dimerization can yield intermolecular charge transfers and, for some cases, excited-state charge transfers.[39–41]

In the context of two π-stacked arenes, C 1s → π* resonant transitions induced by out-of-plane polarized radiation are used as a probe of their intermolecular interaction and thus of the π–π distance.[23] The two arenes of the amino acids shown in Fig. 1 have phenyl and benzol functional groups, respectively. It is shown that intramolecular (local) resonant transitions (orange arrows) can occur in non-paired amino acids, while intermolecular charge transfer transitions (blue arrow) only arise in paired ones. The latter are referred to as non-adiabatic excited-state charge transfer (ESCT). Even without an X-ray excitation, π stacked systems can involve valence-space intermolecular charge transfer,[42,43] sometimes also referred to as transfer doping.[44] Here this is named non-adiabatic ground-state charge transfer (GSCT). The C 1s → π* resonant transitions stem from excited-state calculations by the quantum chemistry software package ORCA[45] using the combination of the restricted open-shell configuration interaction singles (ROCIS) approach with the density functional theory (DFT)[46] employing the functional ωB97M-V/D3BJ.[47]§ The inter-fragment interaction energy for the chemical models was calculated by the quantum chemistry software package GAMESS[48] using the fragment molecular orbital (FMO) method[49] with the spin-component-scaled second-order Møller–Plesset perturbation theory (SCS-MP2).[50] The here derived GSCT energy was calculated using the pair interaction energy decomposition analysis (PIEDA) method.[51,52] After explaining the X-ray absorption calculations in the following section, the details of the theoretical analysis will be given for both the ESCT and the GSCT in the section entitled charge-transfer analysis.

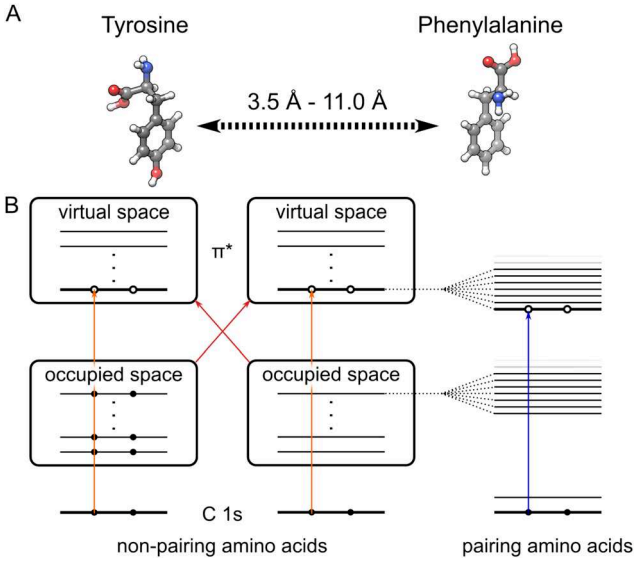

Fig. 1 Representation of the pair of aromatic amino acids and their distance–dependent interactions. (A) Face-to-face π stacking with arene distances ranging from 3.5 to 11.0 Å. (B) Dipole-allowed transitions from core to virtual molecular orbitals. Local excitations within the same amino acid and charge-transfer excitations (ESCT) coupling both amino acids are represented with orange and blue arrows, respectively. Valence-space intermolecular interactions, GSCT, measured as a charge transfer energy, are highlighted with the red crossed arrows.

X-ray absorption calculation

The ESCT associated with the π–π stacking has been theoretically studied in aromatic systems[23,25,26,53] and is measured here through a theoretical analysis of the calculated singly excited state interactions of the core and virtual molecular orbitals (MO) involved in the X-ray excitation, which can generally be computed using configuration interaction singles (CIS)-type wavefunctions for closed-shell[54] or open-shell molecules[55] in combination with DFT including the zero-order regular approximation for relativistic effects.[56] Accounting for both dynamical (from DFT) and non-dynamical (from CIS)

‡ See ESI,† Section S1 and S2.

§ See ESI,† Section S2 for the computational details.

correlation effects on the ground and excited states would also be possible with multireference methods,[57] linear-response, or equation-of-motion coupled cluster methods,[58,59] scaling considerably on the computational cost according to the size of the system. The combination of DFT and CIS-type wave functions also offers both types of dynamic correlation[54,55,57] and further enables the consideration of spin–orbit coupling effects, which may be relevant for open-shell electron configuration systems such as protonated and sulfur-containing molecular structures.[14,16,20,21,60]

In CIS theory, a singly excited state determinant implies the replacement of an occupied orbital ϕ_i by a previously unoccupied orbital ϕ_a. The replacement can be expressed by the second quantization operator $\hat{a}_i^a = \hat{a}_a^\dagger \hat{a}_i$ acting on the ground state. The CIS wave function $|\Psi_{\mathrm{CIS}}\rangle = c_{\mathrm{HF}}\Psi_{\mathrm{HF}} + \sum_{ia} c_i^a \hat{a}_i^a |\Psi_{\mathrm{HF}}\rangle$ is the linear combination of all the singly excited state determinants from its Hartree–Fock (HF) reference determinant. See ref. 46, 54, 57 and 61 for further theoretical details on the construction of the Kohn–Sham (KS) orbitals from DFT in the CIS-type framework for closed- and open-shell electronic structures. As noted here for the restricted open-shell CIS (ROCIS) cases, the study of the ESCT within the DFT/ROCIS framework broadly enables the consideration of closed-shell systems, as is the case for the aimed π–π interaction associated with the aromatic chemical models.

After performing the Löwdin orthonormalization procedure[62] over the DFT/ROCIS space, a set of excited-state eigenfunctions and their associated eigenvalues are obtained from the Hamiltonian matrix ($\hat{\mathbf{H}}^{\mathrm{DFT/ROCIS}}$) by applying the Davidson diagonalization method.[63,64] All the resonant transitions can then be studied from the calculated eigenvalues and eigenvectors. Their transition intensities are in the simplest form obtained *via* the electric dipole moment operator component $\hat{\mu}$ between an initial and a final state multi-electron wavefunction of CIS type ($|\Psi_{\mathrm{CIS}}\rangle$), $|\Psi_I\rangle$ and $|\Psi_F\rangle$. The oscillator strength expressed by $\hat{\mu}$ is $f_{\mathrm{ed}} = |\langle\Psi_I|\hat{\mu}|\Psi_F\rangle|^2$ (see ref. 65 for further details). The transition densities between the initial $|\Psi_I\rangle$ and the final $|\Psi_F\rangle$ states $\rho_{pq}^{IF} = \langle\Psi_F|\hat{E}_p^q|\Psi_I\rangle$ can be expressed in the context of the elements of the CIS matrix in DFT/ROCIS as

$$\rho_{pq}^{IF} = \sum_{\kappa,\lambda}^{\text{CIS basis}} C_{\lambda F}^{*} C_{\kappa I} \left\langle \lambda \middle| \hat{E}_p^q \middle| \kappa \right\rangle, \tag{1}$$

where C is the matrix of coefficients and the excitation operator $\hat{E}_p^q$ stands for a single excitation such as $\hat{a}_p^q$. The coupling of κ and λ can have a different assignation of the basis functions[61] which, for the case of X-ray absorption, only involves excitations from double occupied molecular orbitals (DOMOs) to virtual molecular orbitals (VMOs) as reflected by the excited state CIS function $|\Phi_i^a\rangle$. Moreover, the solution of the transition densities expresses the coupling of orbitals in the core space ϕ_i and orbitals in the virtual space ϕ_a.

Charge-transfer analysis

From the C 1s → π* resonant transitions, the component associated with the ESCT in the π–π stacking is characterized as follows. Transition densities from eqn (1), their intensities, and the Löwdin population of the molecular orbitals involved in the resonant transitions are used. The ROCIS excitation space for closed-shell systems includes only the class DOMO → VMO, see ref. 46 and 61 for details on other types of excitations. The transition density matrix equation uses the single excitation basis function $|\Phi_i^a\rangle$ and it can be written as

$$\rho_{ia}^{n} = \sum_{\kappa,\lambda}^{\text{CIS basis}} C_{\lambda n}^{*} C_{\kappa 0} \langle \lambda | E_i^a | \kappa \rangle. \tag{2}$$

This transition density matrix representation is widely used in excited-state calculation methods such as time-dependent Hartree–Fock (TDHF)[66] and linear-response time-dependent DFT (TDDFT).[66,67] The nomenclature of ρ_{ia}^{IF} from eqn (1) is here changed to ρ_{ia}^{n} considering that the initial state is the ground state and the final state is any one from a set of n excited states with the targeted energy range, *e.g.* of C 1s → π* excitations. The oscillator strength previously expressed as f_{ed} here is also changed to f^n. In each excited state, the transition density matrix ρ_{ia}^{n} comprises the sum of single excitation contributions, normalized to the unit. Scaling each contribution by the oscillator strength of that excited state yields individual oscillator strength values for each contribution, giving γ_{ia}^{n} as

$$\gamma_{ia}^{n} = f^n \cdot \rho_{ia}^{n}. \tag{3}$$

The transition intensity of the n-th excited state can thus be expressed by intensity contributions of the transition density matrix elements, *i.e.* by the importance of the underlying core-virtual coupling orbital contributions. The calculation of the elements in γ_{ia}^{n} applies when the dipole-allowed transitions preserve the ratio of all single excitation contributions.

The same core-to-virtual molecular orbital coupling will contribute to more than one transition density matrix, hence it could be part of several C 1s → π* resonant transitions in a range of excited states [l,m]. This range spans from a minimum, l, to a maximum energy, m, excited state that define the region of a peak of interest having the targeted C 1s → π* resonant transitions. Moreover, the same core-to-virtual molecular orbital coupling provides transition intensities independent of the excited state in which they are involved. Thus, the transition density matrix elements γ_{ia}^{n} of eqn (3) are summed up over the range of excited states [l,m] that are part of the set of n excited states as follows

$$\gamma_{ia}^{[l,m]} = \sum_{n=l}^{m} \gamma_{ia}^{n}. \tag{4}$$

The criteria for selecting an excited-state range [l,m] is that they promote the same type of transition, *e.g.* C 1s → π*. The dimension of the matrix $\gamma_{ia}^{[l,m]}$ also corresponds to the number of core and virtual molecular orbitals. Finally, it is assumed that the Löwdin population[68] of electrons on specific atoms obtained for the ground state can be used to obtain atomic-centered contributions to the electronic transition density as

$$\tilde{\gamma}_{AA'}^{[l,m]} = \mathbf{N}_{A',a} \cdot \left(\gamma_{ia}^{[l,m]} \cdot \mathbf{N}_{A,i} \right), \tag{5}$$

where the density populations $\mathbf{N}_{A',a}$ and $\mathbf{N}_{A,i}$ are evaluated on the atoms A and A' with the core i and virtual a atom-centered basis orbitals. Transition intensities are in this way rescaled by

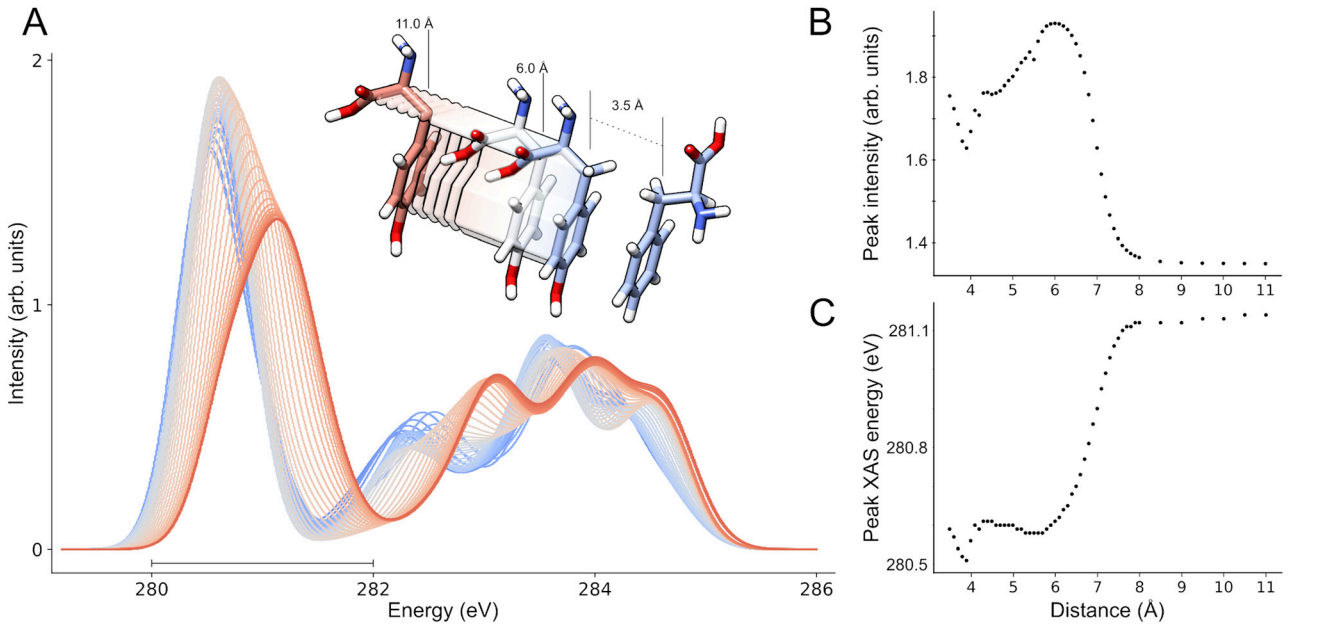

Fig. 2 (A) Set of carbon K-edge XAS spectra for the FY model in the energy range from 279 to 286 eV computed for an intermolecular distance variation from 3.5 (blue) up to 11 Å (red). (B) Evolution of the first peak's maximum intensity (and C: centroid energy) as a function of the π stacking distance.

the population overlap of the atoms in the core (donor) and the virtual space (acceptor). For the case of the C 1s → π* resonant transitions, the $\tilde{\gamma}_{AA'}^{[l,m]}$ dimension corresponds to the number of carbon atoms from the core space and all of the atoms from the virtual space.

The application of the analysis is performed over the calculated C K-edge XAS spectra of the models FY, FW, and WY. The resonant transitions associated to the π–π interactions are characterized by the $\tilde{\gamma}_{AA'}^{[l,m]}$ matrix analysis as the ESCT component of the total of transitions. The implementation of the analysis is available on GitHub for the closed-shell and restricted open-shell cases.¶ Even though the implementation can be applied to TDDFT calculations, the method may underestimate core-electron excitation energies for Rydberg and charge-transfer states[65] when not strictly using long-range hybrid functionals.[47,69] This could be a significant limitation, as the π–π interaction of the chemical models in this study is intended to be measured by their charge-transfer effect in the context of X-ray absorption.

The GSCT of the chemical model is calculated as the charge transfer energy component using the PIEDA method (pair of interfragment energy decomposition analysis).[52,70] Briefly, PIEDA extracts the pair of interaction energy ΔE_{IJ} within the framework of the fragment molecular orbital (FMO) method used to calculate the total of the energy of a chemical system that allows for fragmentation (as *e.g.* a molecular dimer).[49,51] The binding energy of a pair of amino acids, ΔE_{IJ}, can be further decomposed into the electrostatic (ΔE_{es}), exchange (ΔE_{ex}), charge transfer (ΔE_{ct+mix}), dispersion and correlation (ΔE_{di+rc}), and solvent (ΔE_{solv}) components as

$$\Delta E_{IJ} = \Delta E_{es} + \Delta E_{ex} + \Delta E_{ct+mix} + \Delta E_{di+rc} + \Delta E_{solv}. \quad (6)$$

The charge transfer term (ΔE_{ct+mix}, abbreviated here as GSCT) represents the ground-state interfragment interaction involving both the occupied valence and the virtual molecular orbital coupling between the fragments,[43] here the amino acids, *I* and *J*. The delocalization of the interfragmental interactions is computed by the ΔE_{ct+mix},[42] which is exploited to analyse the π-distance effect involved in the chemical model.

Results

The C 1s → π* transitions of X-ray absorption spectra of amino acid pairs are analyzed as a function of their distance to identify ground and excited state charge-transfer contributions arising solely from π–π stacking. For the sake of simplicity, the calculations and analyses are detailed throughout this section only for the Phe–Tyr (FY) model and briefly shown for the other two Phe–Trp (FW) and Tyr–Trp (YW).‖

The carbon K-edge XAS spectra shown in Fig. 2 were calculated for the complete FY set of 52 π-stacking distances ranging from 3.5 to 11.0 Å. The most intense peak of the XAS spectrum is located around 279 to 282 eV (Fig. 2A) and can for all distance be assigned to C 1s → π* transitions, predominantly attributed to the arene carbons. Note that experimentally the C 1s → π* transitions are lying at ∼285.1 eV.[71] Here, the calculated energy is not shifted to fit experimental values. The overall XAS spectral shape is conserved for the entire FY set of systems, regardless of the change in the FY non-covalent distance. However, Fig. 2A shows an overall shift of the complete spectrum to lower energies when the non-covalent

¶ See ESI,† Section S3 for further details.

‖ See ESI,† Section S4 for further details.

distance decreases and the FY system evolves from isolated amino acids to an interacting π stack. As shown in Fig. 2C, the evolution of the centroid energy of the C 1s → π* peak has a sigmoidal trend (except for the shortest distances). Its value is constant above 8.0 Å but sharply decreases by 0.5 eV as the amino acids get closer. As represented in the Fig. 2B and C, we observe that in addition to the energy shift, the maximum intensity of the C 1s → π* transition peak increases by ∼40% as the face-to-face FY distance decreases down to 6.0 Å. Below 6.0 Å the peak intensity decreases slightly to + 30% compared to the isolated case. Both, peak intensity and centroid energy converge as the distance increases above 8.0 Å.

Fig. 3A shows the chemical structure of the FY system at 3.8 Å intermolecular distance, and Fig. 3B shows the $\tilde{\gamma}^{[1,26]}$ matrix plotted as a normalized heatmap. The FY atoms are numbered by atom type and sorted by amino acid (Fig. 3A). This labeling is also used in subsequent heatmaps. Each matrix element of $\tilde{\gamma}^{[l,m]}_{AA'}$ represents the coupling of a carbon atom in the core space A on either of the monomers to any atom A' in the virtual space on the same or the other amino acid. The heatmap of $\tilde{\gamma}^{[l,m]}_{AA'}$ is divided in four submatrices, where those on the diagonal, $\tilde{\gamma}^{[l,m]}_{\text{local}}$, (orange squares) are the intramolecular resonant transition intensities (local excitations of the amino acids) and those on the off-diagonal, $\tilde{\gamma}^{[l,m]}_{\text{non-local}}$, (blue squares) are the intermolecular ones (charge-transfer excitations coupling both amino acids). In the off-diagonal matrices, the C 1s → π* transitions highlighted by the green squares, $\tilde{\gamma}^{[l,m]}_{\pi-\pi}$, represent the coupling of the phenylic carbon atoms of one amino acid with the phenylic carbon atoms of the other amino acid, *i.e.*, the C 1s(F) → π* (Y) and C 1s(Y) → π* (F) transitions. These are the regions in the matrix having the, on average, highest intensities. By looking at

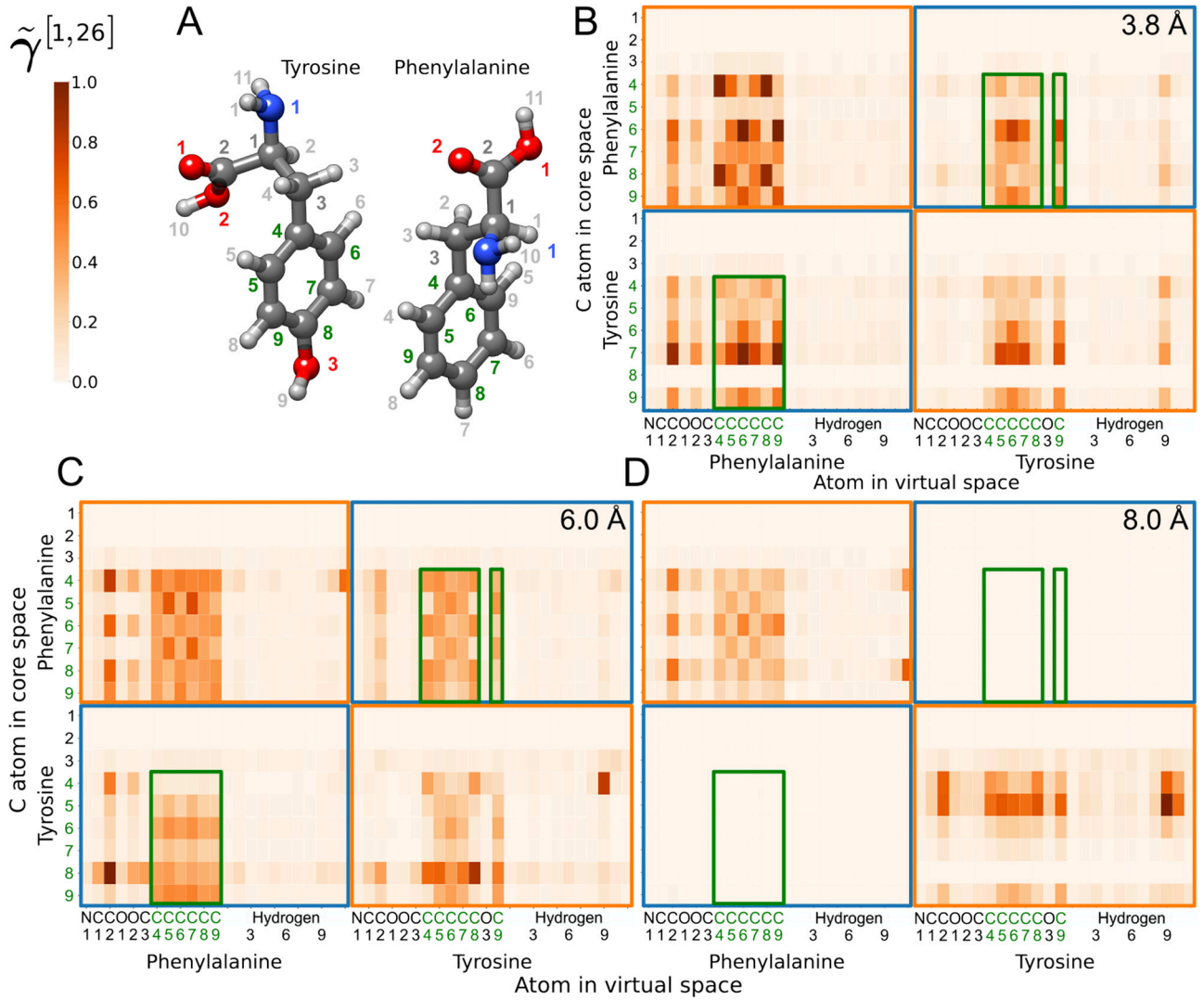

Fig. 3 Representation of the transition intensities in terms of their atomistic contributions using $\tilde{\gamma}^{[l,m]}_{AA'}$. (A) FY system numbered by the atom type. Atom labels in green color correspond to the carbon atoms of the arenes, those in dark gray to the other C atoms. Heatmaps of $\tilde{\gamma}^{[1,26]}$ expressed as relative intensities for all matrix elements, arising from the combination of C and all the atoms, are given for the π stacking distances (B) 3.8 Å, (C) 6.0 Å and (D) 8.0 Å. The local C 1s(F) → π* (F) and C 1s(Y) → π* (Y) resonant transitions are orange-squared, all non-local C 1s(F) → π* (Y) and C 1s(Y) → π* (F) transitions are blue-squared while the charge-transfer transitions associated only to the carbon atoms of the arenes are green-squared.

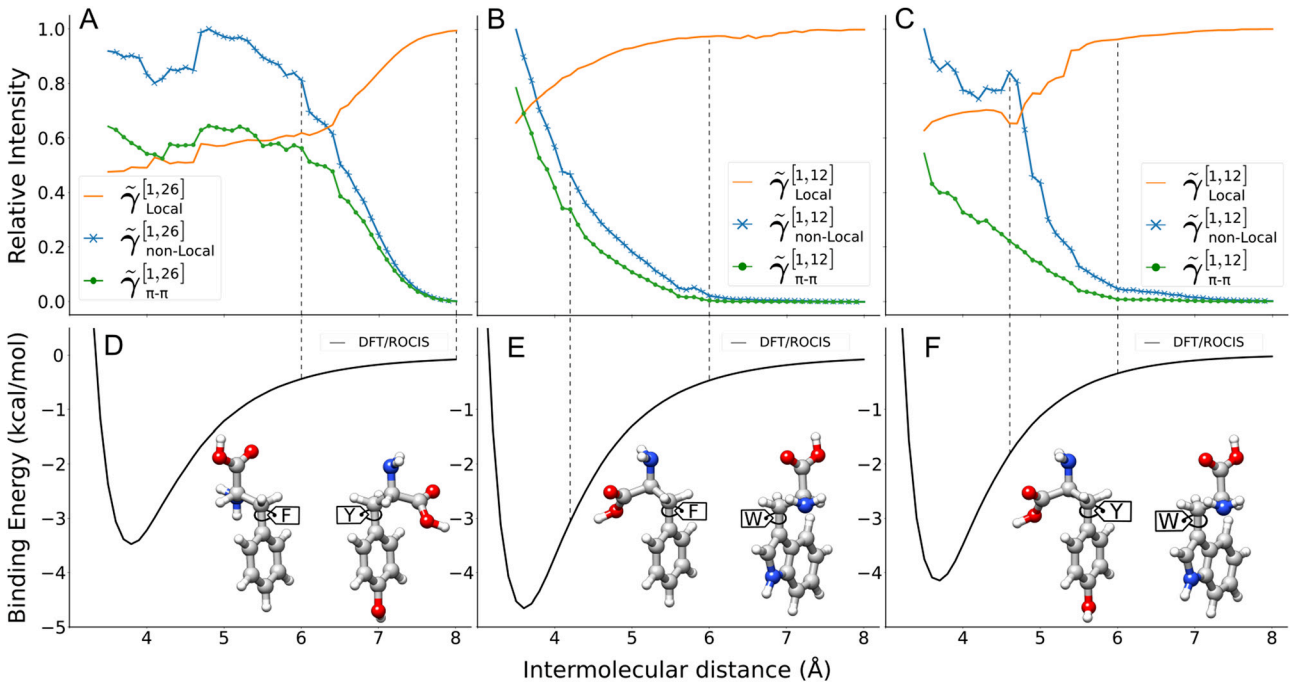

Fig. 4 Intensities of the C 1s → π* transition in the range 279–285 eV as a function of the π-stacking distance expressed in terms of the intramolecular resonant transitions (orange line), intermolecular resonant transitions (blue line), and intermolecular resonant transitions associated with the arenes (green line), for (A) the FY model, (B) the FW model and (C) the YW model. Ground state potential energy curve for (D) FY model, (E) FW model, and (F) YW model.

the two heatmaps of the FY model at 6.0 Å (Fig. 3C) and 8.0 Å (Fig. 3D), one can see that the contributions of the local excitations ($\tilde{\gamma}^{[l,m]}_{\text{local}}$, orange squares) evolve towards dominating over the charge-transfer excitations ($\tilde{\gamma}^{[l,m]}_{\text{non-local}}$, blue squares), which are always dominated by the carbon atoms of the arenes ($\tilde{\gamma}^{[l,m]}_{\pi-\pi}$, green squares) and the carbon and oxygen atoms of the carboxyl functional group (carbon atom with gray 2). In the heatmap at 8.0 Å (Fig. 3D), the disappearance of the intermolecular resonant transitions (green squares) is clear. A similar behavior is found for the two other amino acid pairs.**

In Fig. 4, the comprehensive transitions of intramolecular $\tilde{\gamma}^{[l,m]}_{\text{local}}$ (orange), intermolecular $\tilde{\gamma}^{[l,m]}_{\text{non-local}}$ (blue) and arene-only nature, $\tilde{\gamma}^{[l,m]}_{\pi-\pi}$ (green), for all involved atoms are presented by summation of the matrix elements within these three groups of elements (as laid out separately in Fig. 3B) for each non-covalent distance. The three summation values $\tilde{\gamma}^{[l,m]}_{\text{local}}$, $\tilde{\gamma}^{[l,m]}_{\text{non-local}}$ and $\tilde{\gamma}^{[l,m]}_{\pi-\pi}$ are plotted as function of intermolecular distance for the models FY, FW and YW (Fig. 4A–C). For local excitation intensities in each chemical model, the intramolecular resonant transition curves were normalized to their maximum while for the charge-transfer excitation intensities, the intermolecular $\tilde{\gamma}^{[l,m]}_{\text{non-local}}$ and the intermolecular resonant transitions associated only to the π–π stacking $\tilde{\gamma}^{[l,m]}_{\pi-\pi}$ values were normalized with respect to the maximum value of the intermolecular $\tilde{\gamma}^{[l,m]}_{\text{non-local}}$ curves. Non-normalized results†† show that the $\tilde{\gamma}^{[l,m]}_{\text{local}}$, evaluating the CT governed by inductive effects, is substantially larger than the intermolecular CT $\tilde{\gamma}^{[l,m]}_{\text{non-local}}$ as expected.

The potential energy curves for the FY, FW and YW models (Fig. 4D–F) are plotted exactly below the transition matrix contributions. They show that the dissociation range of the dimer sets on after 6.0 Å. The local and charge-transfer excitation intensities change with respect to the π stacking distance. At the dissociation limit at 8.0 Å (Fig. 4D) for the FY model, there are no transitions from one to the other amino acid: $\tilde{\gamma}^{[l,m]}_{AA'}$ for both intermolecular interactions reaches zero intensity while for the intramolecular interactions it reaches its maximum (Fig. 4A). For the FW and YW models (Fig. 4B and C) the intermolecular interactions already drop at slightly shorter distances, namely at 6.0 Å. They reach zero at the dissociation limit (Fig. 4E and F). For all three models in Fig. 4, the charge-transfer excitation intensity (from $\tilde{\gamma}^{[l,m]}_{\text{non-local}}$ and $\tilde{\gamma}^{[l,m]}_{\pi-\pi}$) is highest around the binding energy minimum (~3.8 Å).

The charge-transfer excitations in the FY model (Fig. 4A) are associated to the coupling between both arenes and the coupling of the aromatic rings with the carboxyl groups of the neighboring amino acid. For the FW model (Fig. 4B), the contributions are mostly from the carbon atoms of both aromatic rings. Lastly, in the YW model (Fig. 4C), the contributions mostly correspond to the carbon atoms of the aromatic ring of the tyrosine to the atoms of the carboxyl group the the tryptophan, which is displayed at the region of 4.6 Å. These charge-transfer excitations represent the non-adiabatic excited state charge transfer (ESCT) that occurs by coupling both amino acids from their π-stacked atoms. In the FY and YW models,

** *Cf.* ESI,† Section S4 and Fig. S8, S9.
†† *Cf.* ESI,† Section 4, Fig. S10.

ESCT shows that tyrosine contributes more than phenylalanine and tryptophan acting as a donor in the C 1s → π* resonant transitions.‡‡

From the binding energy (ΔE_{IJ}) calculated by the PIEDA method,§§ one can obtain the charge transfer energy ($\Delta E_{\mathrm{ct+mix}}$), referred here as non-adiabatic ground state charge transfer (GSCT). In Fig. 5, the GSCT (red) and the ESCT associated only to $\tilde{\gamma}^{[l,m]}_{\pi-\pi}$ (green) show an inverse convergence pattern with respect to the pair of amino acids π stacking distances. The three models have an asymptotic trend of the $\Delta E_{\mathrm{ct+mix}}$ from negative values to zero after the dissociation range distance of 6.0 Å. Inflection points can be observed in the region of ∼4 to 5 Å of the the asymptotic trends, where in the FY model one is more prominent (Fig. 5A) than in the other two models (Fig. 5B and C). The calculated $\Delta E_{\mathrm{ct+mix}}$ measures intermolecular interactions at the ground state between the valence space of the aromatic side chains of both amino acids in larger distances that those at the minimum non-covalent binding energy (Fig. 4D–F). The ESCT component $\tilde{\gamma}^{[l,m]}_{\pi-\pi}$ in the models FW (Fig. 5B) and YW (Fig. 5C) converges in the dissociation range (6.0 Å) in contrast to the FY (Fig. 5A) (8.0 Å). Both, the GSCT $\Delta E_{\mathrm{ct+mix}}$ and the ESCT $\tilde{\gamma}^{[l,m]}_{\pi-\pi}$ drop equally fast regardless the physical dimensions, one in energy and the other in relative intensity.

Discussion

Core-to-valence excitations are decomposed into atomic contributions to the electronic transition density matrix $\tilde{\gamma}^{[l,m]}_{AA'}$. Applying this decomposition to the amino acid base pairs Phe–Trp (FW model), Tyr–Trp (YW), and Phe–Tyr (FY) enables to differentiate local excitations within one amino acid from intermolecular charge-transfer excitations coupling both amino acids. The intermolecular transitions sensitively depend on the π stacking of the arenes. As we observed for the FW, YW and FY models—and others evidenced theoretically in the case of phthalocyanine dimer[23]—hypsochromic shifts in the C 1s → π* transition energies and intensity variations arise when the non-covalent π stacking distance changes. Especially in the FY model (Fig. 2C), two regimes can be distinguished: at distances lower than 6.0 Å, the energy of the C 1s → π* transition is nearly constant, where the FY model is stably, non-covalently bonded (Fig. 4D). At larger distances, the energy converges to a higher values, while the amino acid pair dissociates. These two regimes are not as distinct for the other two models.¶¶ They display larger ground state binding energies at non-covalent binding distances (Fig. 4E and F).

Atomic contributions to the $\tilde{\gamma}^{[l,m]}_{AA'}$ matrix elements are classified by chemical groups in the amino acids as shown in the heatmaps in Fig. 3,‖‖ exploiting the localized nature of the core molecular orbitals involved in the transitions of the XAS process.

‡‡ See ESI,† Section S4 for further details.
§§ See ESI,† Section S2 for the computational details.
¶¶ See ESI,† Section S4 and Fig. S2.C, S3.C.
‖‖ See ESI,† Section S4 and Fig. S4–S9 for further details.

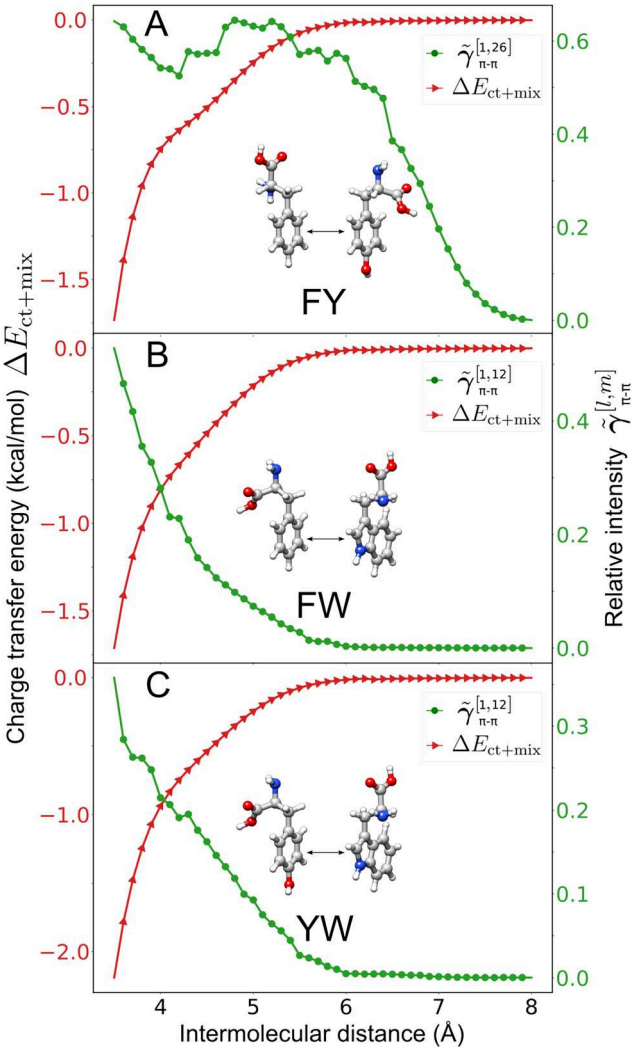

Fig. 5 Comparison of the ground state charge transfer (red, negative values on left axis) and excited state charge transfer (green, positive values on right axis) with respect to the non-covalent distance for the FY, FW and YW systems.

The dispersed electronic density in the valence space is exploited by clustering the carbon atoms of the conjugated aromatic rings to measure the contributions of the phenyl functional group of phenylalanine (F) and tyrosine (Y) and the indol functional group of tryptophan (W) to the transitions. The peptide bond may influence the transition intensities between the arenes in the side chains, however here it is deprecated since the chosen chemical model only has non-covalent interactions. $\tilde{\gamma}^{[l,m]}_{AA'}$ expresses the π stacking change as a single property independent of avoiding other factors such as backbone-side chain and non-related aromatic–aromatic interactions or conformational isomers. At non-covalent binding distances, the contribution of the intramolecular ($\tilde{\gamma}^{[l,m]}_{\mathrm{local}}$, local excitations) and intermolecular ($\tilde{\gamma}^{[l,m]}_{\mathrm{non\text{-}local}}$, charge-transfer excitations) transition intensities thus reflects the changes in the delocalization of the electronic density between two aromatic rings. Moreover, at non-covalent distances in the dissociation range, local excitations mostly

reflect the behavior of the π interactions of the isolated arenes. Our work suggests that the π stacking can be studied by analysing the atomic contribution of the transitions associated to the phenyl and indol functional groups along the elements of $\tilde{\gamma}^{[l,m]}_{AA'}$.

Evaluation of $\tilde{\gamma}^{[l,m]}_{AA'}$ can also be performed using other obtained transition density matrices, such as those from TDHF and TDDFT methods, along with population density analyses like Mulliken charges or the Löwdin population presented here. For other systems in higher excited states, distinguishing exclusive C 1s → π* transitions from the C 1s → σ* transitions could be challenging, posing a drawback for evaluating $\tilde{\gamma}^{[l,m]}_{AA'}$ when focusing solely on the aimed π–π stacking interaction of aromatic rings. The defined atomic-centered contributions of $\tilde{\gamma}^{[l,m]}_{AA'}$ provide a flexible definition of chemical regions—$\tilde{\gamma}^{[l,m]}_{\text{non-local}}$, $\tilde{\gamma}^{[l,m]}_{\text{local}}$ and $\tilde{\gamma}^{[l,m]}_{\pi-\pi}$—which mitigates potential limitation in the excited-state selection range. The nature of conjugated aromatic rings restricts the definition of the chemical region (A and A'): atoms belonging to an aromatic ring cannot be separated into several subregions due to the delocalized nature of the π* orbitals.[15]

The π–π stacked arrangement appears to be favored by the ESCT over other common spatial conformations in *ab initio* molecular dynamics.[25,26] In the FW and YW models, this parallelly displaced arrangement enables orbital overlap between the phenyl and the pyrrol ring of the indol group. For FY, the π–π stacking has been modeled within an eclipsed conformation between both arenes (all bonds are parallel), promoting a high orbital overlap between the p orbitals spatially oriented outward the plane of both phenyl groups. Delocalized virtual molecular orbitals along the π-conjugated systems provide a higher orbital overlap enhancing intermolecular charge-transfer processes.[72] For instance, the intermolecular transition intensities $\tilde{\gamma}^{[l,m]}_{\pi-\pi}$ (as the excited state charge-transfer component) of the FY model stays at higher values along the non-covalent binding distance due to the strong orbital overlap in FY in comparison to the FW and YW models. In other charge-transfer processes, the delocalized virtual molecular orbitals in the π–π stacking space enhance a strong interaction with the occupied orbitals. This interaction in the valence space can be measured as a ground-state charge transfer (GSCT) energy component $\Delta E_{\text{ct+mix}}$. Interacting arenes yield intermolecular charge-transfer effects when the interaction is at closer distances than 4 Å,[72,73] which is notoriously observed for the models having an inductive effect on the aromatic ring due to the hydroxyl group in tyrosine. In highly conjugated systems, charge transfer governed by inductive effects is measured as density differences between the ground and excited states, showing a strong dependence on the interaction distance.[53] The charge transfer energy calculated here has a similar trend (Fig. 5), decreasing as the π–π interaction distance separation increases as it is expected.[22,32]

Conclusions

In this work, we developed a theoretical analysis of the core–hole resonant transitions observed in the X-ray absorption processes, regarding the atomic contributions in the electronic transition density matrix and correlated it with the ground state interaction properties. The intermolecular resonant transitions associated to the side chain aromatic π–π stacking (ESCT) and the intermolecular valence space interaction (GSCT) could be correlated to the distance between the side chains. The method was applied to pairs of aromatic amino acids to understand the influence of the π stacking distance on the intermolecular charge-transfer contributions, ground-state charge-transfer $\Delta E_{\text{ct+mix}}$ and excited-state charge-transfer $\tilde{\gamma}^{[l,m]}_{\pi-\pi}$. On the one hand, the $\tilde{\gamma}^{[l,m]}_{\pi-\pi}$ matrix elements reflect the π stacking interaction between the aromatic side chains, *via* the C 1s → π* transitions. On the other hand, the GSCT component represents the coupling between the occupied and unoccupied valence molecular orbitals of two amino acids, which includes those entangled in the aromatic region. We can quantify the loss of charge transfer energy, as a GSCT component, along with the intensity loss of the intermolecular C 1s → π* resonant transitions, as an ESCT component, when the π stacking distance is getting larger. This work suggests that the analysis of charge transfer energy as C 1s → π* resonant transition could be used to determine threshold criteria for the π−π interaction between aromatic amino acids in larger molecules.

Author contributions

S. B., L. S. did the conceptualization of the chemical interaction. C. M. did the conceptualization of the theoretical model and its theoretical development under the supervision of R. M. and A. B. C. M. did the computational calculations under the supervision of L. S., S. B. and R. M. C. M. did the formal analysis and research process under the supervision of S. B., R. M. and A. B. C. M. did the code implementation of the theoretical analysis, methodology and supporting algorithms. C. M. and J. L. did the test of the codes and their verification for the overall reproducibility of results. All authors participated to review and edit the original draft written by C. M.

Data availability

The data, codes and analysis supporting this article have been included as part of the ESI.†

Conflicts of interest

There are no conflicts to declare.

Acknowledgements

This work is supported by the Data Science in Hamburg – HELMHOLTZ Graduate School for the Structure of Matter, DASHH, grant no. HIDSS-0002. C. M. and A. B. like to thank the HIDA Trainee Network program for financing a stay of C. M. at HZB in 2023. The authors would like to thank the DESY and JFZ computing centres for providing computing resources. A. B. and R. M. thank the Impuls– und Vernetzungsfonds of the Helmholtz– Gemeinschaft for the Helmholtz-AI project

AI-4-XAS. J. L. acknowledges funding from the Centre for Molecular Water Science (CMWS) in an Early Science Project and the Région Normandie (France) within the NANOHYDRAD project. L. S. and S. B. acknowledge funding by the Helmholtz Initiative and Networking Fund. S. B. acknowledges support from the BMBF (Grant No. 13K22CHA) and the Cluster of Excellence 'CUI: Advanced Imaging of Matter' of the Deutsche Forschungsgemeinschaft (DFG) – EXC 2056 – project ID 390715994.

Notes and references

1 S. Burley and G. A. Petsko, *Science*, 1985, **229**, 23–28.
2 E. A. Meyer, R. K. Castellano and F. Diederich, *Angew. Chem., Int. Ed.*, 2003, **42**, 1210–1250.
3 R. M. Vernon, P. A. Chong, B. Tsang, T. H. Kim, A. Bah, P. Farber, H. Lin and J. D. Forman-Kay, *eLife*, 2018, **7**, e31486.
4 D. A. Dougherty, *Acc. Chem. Res.*, 2013, **46**, 885–893.
5 J. L. Asensio, A. Ardá, F. J. Cañada and J. Jimenez-Barbero, *Acc. Chem. Res.*, 2013, **46**, 946–954.
6 F. U. Hartl, A. Bracher and M. Hayer-Hartl, *Nature*, 2011, **475**, 324–332.
7 J. Boese, A. Osanna, C. Jacobsen and J. Kirz, *J. Electron Spectrosc. Relat. Phenom.*, 1997, **85**, 9–15.
8 Y. Zubavichus, A. Shaporenko, M. Grunze and M. Zharnikov, *Nucl. Instrum. Methods Phys. Res., Sect. A*, 2009, **603**, 111–114.
9 Y. Zubavichus, A. Shaporenko, M. Grunze and M. Zharnikov, *J. Phys. Chem. B*, 2007, **111**, 9803–9807.
10 J. Stewart-Ornstein, A. P. Hitchcock, D. Hernández Cruz, P. Henklein, J. Overhage, K. Hilpert, J. D. Hale and R. E. Hancock, *J. Phys. Chem. B*, 2007, **111**, 7691–7699.
11 X. Liu, F. Zheng, A. Jürgensen, V. Perez-Dieste, D. Petrovykh, N. Abbott and F. Himpsel, *Can. J. Chem.*, 2007, **85**, 793–800.
12 R. A. Metzler, R. M. Olabisi, M. Abrecht, D. Ariosa, C. J. Johnson, B. Gilbert, B. H. Frazer, S. N. Coppersmith and P. Gilbert, *AIP Conference Proceedings*, 2007, pp. 51–55.
13 J. Yano and V. K. Yachandra, *Photosynth. Res.*, 2009, **102**, 241–254.
14 S. Dörner, L. Schwob, K. Atak, K. Schubert, R. Boll, T. Schlatholter, M. Timm, C. Bülow, V. Zamudio-Bayer and B. von Issendorff, *et al.*, *J. Am. Soc. Mass Spectrom.*, 2021, **32**, 670–684.
15 Y. Zubavichus, A. Shaporenko, M. Grunze and M. Zharnikov, *J. Phys. Chem. B*, 2008, **112**, 4478–4480.
16 D. Egorov, S. Bari, R. Boll, S. Dörner, S. Deinert, S. Techert, R. Hoekstra, V. Zamudio-Bayer, R. Lindblad and C. Bülow, *et al.*, *J. Am. Soc. Mass Spectrom.*, 2018, **29**, 2138–2151.
17 O. González-Magaña, G. Reitsma, M. Tiemens, L. Boschman, R. Hoekstra and T. Schlathölter, *J. Phys. Chem. A*, 2012, **116**, 10745–10751.
18 M. F. Tesch, R. Golnak, F. Ehrhard, D. Schön, J. Xiao, K. Atak, A. Bande and E. F. Aziz, *Chem. – Eur. J.*, 2016, **22**, 12040–12049.
19 F. Weber, J. Ren, T. Petit and A. Bande, *Phys. Chem. Chem. Phys.*, 2019, **21**, 6999–7008.
20 L. Schwob, S. Dorner, K. Atak, K. Schubert, M. Timm, C. Bulow, V. Zamudio-Bayer, B. von Issendorff, J. T. Lau and S. Techert, *et al.*, *J. Phys. Chem. Lett.*, 2020, **11**, 1215–1221.
21 X. Wang, S. Rathnachalam, K. Bijlsma, W. Li, R. Hoekstra, M. Kubin, M. Timm, B. von Issendorff, V. Zamudio-Bayer and J. T. Lau, *et al.*, *Phys. Chem. Chem. Phys.*, 2021, **23**, 11900–11906.
22 A. Batra, G. Kladnik, H. Vázquez, J. S. Meisner, L. Floreano, C. Nuckolls, D. Cvetko, A. Morgante and L. Venkataraman, *Nat. Commun.*, 2012, **3**, 1086.
23 M. Linares, S. Stafström and P. Norman, *J. Chem. Phys.*, 2009, **130**, 104305.
24 J. Wang, R. Lv, S. Song, L. Wei, S. Huang, Q. Zhang and K. Wang, *Cryst. Growth Des.*, 2024, **24**, 4114–4121.
25 F. Coppola, P. Cimino, F. Perrella, L. Crisci, A. Petrone and N. Rega, *J. Phys. Chem. A*, 2022, **126**, 7179–7192.
26 F. Coppola, P. Cimino, A. Petrone and N. Rega, *J. Phys. Chem. A*, 2024, **128**, 1620–1633.
27 R. L. Dunbrack Jr, *Curr. Opin. Struct. Biol.*, 2002, **12**, 431–440.
28 J.-L. Brédas, D. Beljonne, V. Coropceanu and J. Cornil, *Chem. Rev.*, 2004, **104**, 4971–5004.
29 X.-Y. Li, X.-S. Tang and F.-C. He, *Chem. Phys.*, 1999, **248**, 137–146.
30 L. Wang, G. Nan, X. Yang, Q. Peng, Q. Li and Z. Shuai, *Chem. Soc. Rev.*, 2010, **39**, 423–434.
31 J.-L. Brédas, J. P. Calbert, D. da Silva Filho and J. Cornil, *Proc. Natl. Acad. Sci. U. S. A.*, 2002, **99**, 5804–5809.
32 V. Coropceanu, J. Cornil, D. A. da Silva Filho, Y. Olivier, R. Silbey and J.-L. Brédas, *Chem. Rev.*, 2007, **107**, 926–952.
33 C. Wang, H. Dong, W. Hu, Y. Liu and D. Zhu, *Chem. Rev.*, 2012, **112**, 2208–2267.
34 C. Janiak, *J. Chem. Soc., Dalton Trans.*, 2000, 3885–3896.
35 K. Kobayashi, H. Masu, A. Shuto and K. Yamaguchi, *Chem. Mater.*, 2005, **17**, 6666–6673.
36 C. Wu, W. Liu, K. Li, G. Cheng, J. Xiong, T. Teng, C.-M. Che and C. Yang, *Angew. Chem., Int. Ed.*, 2021, **60**, 3994–3998.
37 C. Zhang, J. Cheng, Q. Wu, S. Hou, S. Feng, B. Jiang, C. J. Lambert, X. Gao, Y. Li and J. Li, *J. Am. Chem. Soc.*, 2023, **145**, 1617–1630.
38 E. Spuling, N. Sharma, I. D. Samuel, E. Zysman-Colman and S. Bräse, *Chem. Commun.*, 2018, **54**, 9278–9281.
39 K.-L. Woon, C.-L. Yi, K.-C. Pan, M. K. Etherington, C.-C. Wu, K.-T. Wong and A. P. Monkman, *J. Phys. Chem. C*, 2019, **123**, 12400–12410.
40 H. Tsujimoto, D.-G. Ha, G. Markopoulos, H. S. Chae, M. A. Baldo and T. M. Swager, *J. Am. Chem. Soc.*, 2017, **139**, 4894–4900.
41 S. Shao, J. Hu, X. Wang, L. Wang, X. Jing and F. Wang, *J. Am. Chem. Soc.*, 2017, **139**, 17739–17742.
42 M. J. Phipps, T. Fox, C. S. Tautermann and C.-K. Skylaris, *Chem. Soc. Rev.*, 2015, **44**, 3177–3211.
43 K. Yamada and N. Koga, *Theor. Chem. Acc.*, 2012, **131**, 1–17.
44 T. Kirschbaum, T. Petit, J. Dzubiella and A. Bande, *J. Comput. Chem.*, 2022, **43**, 923–929.
45 F. Neese, F. Wennmohs, U. Becker and C. Riplinger, *J. Chem. Phys.*, 2020, **152**, 224108.

46 M. Roemelt, D. Maganas, S. DeBeer and F. Neese, *J. Chem. Phys.*, 2013, **138**, 204101.
47 N. Mardirossian and M. Head-Gordon, *J. Chem. Phys.*, 2016, **144**, 214110.
48 M. S. Gordon and M. W. Schmidt, *Theory and applications of computational chemistry*, Elsevier, 2005, pp. 1167–1189.
49 D. G. Fedorov, *Wiley Interdiscip. Rev.: Comput. Mol. Sci.*, 2017, **7**, e1322.
50 R. Krishnan, J. S. Binkley, R. Seeger and J. A. Pople, *J. Chem. Phys.*, 1980, **72**, 650–654.
51 K. Kitaura, E. Ikeo, T. Asada, T. Nakano and M. Uebayasi, *Chem. Phys. Lett.*, 1999, **313**, 701–706.
52 D. G. Fedorov and K. Kitaura, *J. Comput. Chem.*, 2007, **28**, 222–237.
53 L. Huet, A. Perfetto, F. Muniz-Miranda, M. Campetella, C. Adamo and I. Ciofini, *J. Chem. Theory Comput.*, 2020, **16**, 4543–4553.
54 S. Grimme, *Chem. Phys. Lett.*, 1996, **259**, 128–137.
55 D. Maganas, M. Roemelt, M. Hävecker, A. Trunschke, A. Knop-Gericke, R. Schlögl and F. Neese, *Phys. Chem. Chem. Phys.*, 2013, **15**, 7260–7276.
56 E. v Van Lenthe, J. Snijders and E. Baerends, *J. Chem. Phys.*, 1996, **105**, 6505–6516.
57 S. Grimme and M. Waletzke, *J. Chem. Phys.*, 1999, **111**, 5645–5655.
58 H. Sekino and R. J. Bartlett, *Int. J. Quantum Chem.*, 1984, **26**, 255–265.
59 F. Hampe and S. Stopkowicz, *J. Chem. Theory Comput.*, 2019, **15**, 4036–4043.
60 J. Leroux, J.-Y. Chesnel, C. A. Ortiz-Mahecha, A. Nair, B. Oostenrijk, L. Pille, F. Trinter, L. Schwob and S. Bari, *Chem. – Eur. J.*, 2025, e202403665.
61 M. Roemelt and F. Neese, *J. Phys. Chem. A*, 2013, **117**, 3069–3083.
62 P.-O. Löwdin, *J. Chem. Phys.*, 1950, **18**, 365–375.
63 E. R. Davidson, *J. Comput. Phys.*, 1975, **17**, 87–94.
64 G. L. Sleijpen and H. A. Van der Vorst, *SIAM Rev.*, 2000, **42**, 267–293.
65 S. D. George, T. Petrenko and F. Neese, *Inorg. Chim. Acta*, 2008, **361**, 965–972.
66 A. Dreuw and M. Head-Gordon, *Chem. Rev.*, 2005, **105**, 4009–4037.
67 M. E. Casida, *J. Mol. Struct.: THEOCHEM*, 2009, **914**, 3–18.
68 G. Bruhn, E. R. Davidson, I. Mayer and A. E. Clark, *Int. J. Quantum Chem.*, 2006, **106**, 2065–2072.
69 Y. Zhao and D. G. Truhlar, *J. Phys. Chem. A*, 2006, **110**, 13126–13130.
70 K. Kitaura and K. Morokuma, *Int. J. Quantum Chem.*, 1976, **10**, 325–340.
71 Y. Zubavichus, A. Shaporenko, M. Grunze and M. Zharnikov, *J. Phys. Chem. A*, 2005, **109**, 6998–7000.
72 G. Demirel, R. L. Gieseking, R. Ozdemir, S. Kahmann, M. A. Loi, G. C. Schatz, A. Facchetti and H. Usta, *Nat. Commun.*, 2019, **10**, 5502.
73 A. Rochefort, R. Martel and P. Avouris, *Nano Lett.*, 2002, **2**, 877–880.